Flow, Turbulence and Combustion (2025) 114:941–965
https://doi.org/10.1007/s10494-025-00635-w

RESEARCH

Numerical Simulation of the Agglomeration Behaviour of Spheroidal Particle Pairs in Chaotic Flows

Jacob P. Anderson[1] · Lee F. Mortimer[1] · Timothy N. Hunter[1] · Jeffrey Peakall[2] · Michael Fairweather[1]

Received: 6 May 2024 / Accepted: 2 January 2025 / Published online: 24 February 2025

Abstract

Interactions between attractive spheroidal particles are studied in boxes of chaotic flow under the action of a homogeneous and isotropic forcing technique. The fully resolved fluid field and structure-resolved particle–fluid coupling regime are obtained through direct numerical simulation and an immersed boundary method. Agglomeration outcomes are accommodated through attractive van der Waals forces, suitably adapted to consider the orientational dependencies associated with the non-spherical shape. Binary particle interactions are first studied in quiescent conditions, as well as in a periodic box of chaotic fluid flow. The latter is forced using a stochastic method, where the magnitude of the velocity fluctuations and Taylor–Reynolds number are chosen based on those typically seen in nuclear waste processing scenarios. Differences in particle interaction behaviours are presented for the cases of disks and needles, with the role of orientation and kinetic energy in determining interaction outcomes analysed and contrasted with spheres. Results indicate that needles have the highest agglomeration propensity in the chaotic fluid, followed by spheres, and then disks. Lastly, the inclusion of attractive orientationally-dependent interaction forces promotes alignment between the symmetry axes of spheroidal particle pairs, whilst the increased action of the fluid was also seen to promote alignment between the interacting particles when compared to the quiescent case.

Keywords Multiphase flow · Non-spherical particles · Particle agglomeration · Homogeneous and isotropic turbulence · Immersed boundary method

✉ Jacob P. Anderson
scjpa@leeds.ac.uk

Lee F. Mortimer
l.f.mortimer@leeds.ac.uk

Timothy N. Hunter
t.n.hunter@leeds.ac.uk

Jeffrey Peakall
j.peakall@leeds.ac.uk

Michael Fairweather
m.fairweather@leeds.ac.uk

[1] School of Chemical and Process Engineering, University of Leeds, Leeds LS2 9JT, UK

[2] School of Earth and Environment, University of Leeds, Leeds LS2 9JT, UK

1 Introduction

The interaction behaviours of micron-scale particles in turbulence are relevant in many industrial settings. One important example is found in the nuclear industry, where legacy nuclear waste is kept in storage ponds and silos awaiting transport to more sustainable long-term storage locations (Trojanowicz et al. 2018). During this interim period, nearby particles experiencing approximately quiescent conditions in a liquid interact with one another to form complex agglomerates. Later, in their pipe-based transportation to safer interim storage locations, the turbulent flow can augment the agglomeration process via increased collision frequency. This poses a potential risk, since larger particles are more likely to deposit on the wall or restrict the flow (Wolde et al. 2023), potentially leading to pipe blockages which are expensive to rectify. Also of interest is the reduced pumping efficiency which incurs an indirect cost. A deeper understanding of such processes is therefore of great value to improved process and equipment design.

Multiphase flows containing solids in liquid or gaseous phases are well studied in the literature, with a large amount of work existing on particle-laden flows in canonical geometries (Soldati and Marchioli 2009; Balachandar and Eaton 2010; Kuerten 2016) as well as in more abstract situations such as homogeneous and isotropic turbulence (Elghobashi and Truesdell 1989; Squires and Eaton 1991). This prolonged scientific effort is driven at least in part by the direct applicability of such flows to a breadth of industrial and environmental processes, like those described earlier.

Often, multiphase flows will be turbulent due to the presence of high flow rates and low viscosity fluid media, with a coupled interaction occurring between the turbulence field of the flow and the particles within. The turbulence's chaotic dynamics and the inter-reliant particle positions, orientations, and velocities creates a multiplex system that can be difficult to study. As such, much of the numerical literature focuses on interactions between spherical particles, in turn allowing simplifications to both the modelling and simulation stages. Those studies have proven to be very effective, generating insight on interesting effects in the bulk flow such as preferential concentration (Eaton and Fessler 1994) and turbophoresis (Marchioli et al. 2008) or, pertinently to the present work, turbulent agglomeration behaviour between adhesive particles (Chen et al. 2019).

The use of a spherical assumption is particularly prevalent for four-way coupled regimes, where non-spherical particle collisions must otherwise be computed, posing a notorious challenge, which is covered comprehensively in a review of the literature by Jain et al. (2022) who also propose a solution to the problem in the form of an ellipsoidal collision model. Real industrial processes will most often contain non-spherical particles, and the characteristics of such particles in terms of their dynamics and interactions are much more intricate (Voth and Soldati 2017), as well as more challenging to capture accurately in a numerical simulation (Mandø et al. 2007). One way to include non-sphericity to such a model is through the use of an immersed boundary method (Peskin 2002), where the mesh itself represents the non-spherical shape. This has proved successful in recent years paired with a rigid body assumption (Uhlmann 2005; Mark and van Wachem 2008; Mortimer and Fairweather 2021) but it raises the computational cost significantly, when compared with typical point-particle methods, and this currently limits the number of particles that can be reasonably included.

As well as non-sphericity, certain industrial processes – depending on the particle length scales and chemical or material properties present – are subject to agglomeration processes, further complicating the system. Ho and Sommerfield (2002) demonstrated the

importance of modelling agglomeration effects due to the influence on the carrier-phase as well as the natural impact on the Stokes number distribution of the particle-phase. Similarly, Shardt and Derksen (2012) simulated dense suspensions of red blood cells with resolution of their non-spherical bi-concave shape. In their findings, an order of magnitude difference was observed in sedimentation rate when compared to a reference medical experiment. This was attributed to an absence of agglomeration-inducing forces.

Current methodologies for particle agglomeration in multiphase flows often rely on single timestep determinations based upon the kinetic energy of a pair of colliding particles (e.g. Breuer and Almohammed 2015; Mortimer et al. 2020), with implementations of such effects typically appearing in Lagrangian particle tracking (LPT) or coupled discrete element method frameworks. Colliding particles found to have low kinetic energies in the reference frame of the collision will combine under these models to form an agglomerate as part of the collisional step, at which point a larger point-particle typically replaces the two agglomerating point-particles, such that either volume or inertia is preserved (Almohammed 2018). This is an effective way to incorporate agglomeration into the model, recreating bulk behaviour, but missing some of the time-dependent effects involved in the agglomeration process which arise due to processes acting on very short length and time scales. It is possible that these effects have an impact on the overall multiphase system and so their resolution is of interest to developing general scientific understanding. Moreover, and particularly for non-spherical particles, the morphology of the aggregated particles will almost certainly affect the dynamics of the system at some level, since different non-spherical shapes display very different dynamic behaviours (Njobuenwu and Fairweather 2015; Voth and Soldati 2017). Therefore, it is of importance to resolve the shape of the formed agglomerates as well as the process itself. By understanding the aggregated structures formed in the agglomeration process, the development of lower fidelity models that seek to approximate the process can be informed in more detail, allowing for more cognisant modelling choices; for example, in implementing drag coefficients for agglomerated particles, or choosing an appropriate shape to replace two agglomerated particles with.

Agglomeration can be modelled as an emergent phenomenon arising from the inclusion of attractive van der Waals (vdW) forces. Consideration of the balance between these forces and the repulsive electric double layer (EDL) in a liquid medium is covered by DLVO theory (Derjaguin and Landau 1941; Verwey and Overbeek 1955). The combination of these two forces gives rise to a potential that is a function of the inter-surface separation distance between a particle pair. In order to agglomerate, a pair of approaching particles must first have sufficient kinetic energy to overcome the potential barrier arising from the repulsive EDL force. Beyond this barrier, as the particles move closer still, there lies an attractive potential well. If the post-collision kinetic energy of a colliding particle pair is too low for the particles to escape the well, then they remain bound and an agglomerate is formed.

Everaers and Ejtehadi (2003) and Schiller et al. (2011) derived equivalent expressions to represent the DLVO potential between non-spherical particles as a function of relative orientation, whilst Fujita and Yamaguchi (2007) included the relevant spherical potential into time-dependent nanoparticle simulations. Building upon the latter approach, DLVO forces were included by Mortimer and Fairweather (2021) into an immersed boundary framework representing spheres with diameter 100μm. In the present work, we have combined these approaches to model our non-spherical system.

In LPT studies, it has been observed that agglomeration rates differ across regions of a channel flow, owing to the different turbulence properties found in the various flow regions (Mortimer et al. 2020). This underscores the influence that turbulence has on

agglomeration propensity and so it is of interest to study this interplay in more detail. The cited study aimed to model nuclear waste processing systems and therefore chose calcite particles interacting in water as an appropriate nuclear waste analogue. In the present work, those same properties are used again to bring industrial relevance to the findings, with the aim to complement previous work by interrogating particle interaction behaviours at a more fundamental level.

Periodic boxes of homogeneous and isotropic turbulence (HIT) provide the opportunity to study particle interactions in turbulence in a small simulation domain, giving access to detailed fluid physics at the particle scale. HIT in triply periodic boxes means the lack of a shear-inducing mechanism that can naturally generate turbulence, and so the boxes require a forcing method. Typically, this involves the addition of a source term to the fluid equations. One widely used method is that of Lundgren (2003) who introduced a forcing term proportional to the local velocity field. The class of methods that have followed this approach are known as linear forcing schemes, for example that of Rosales and Meneveau (2005). Lundgren's approach is simple to implement and effective at producing turbulence. As such, it has been widely used but is limited in its application and robustness (Lucci et al. 2010; Mallouppas et al. 2013; Janin et al. 2021). In contrast, the work of Eswaran and Pope (1988) and Alvelius (1999) are two examples of approaches that generate the forcing field independently of the resolved fluid velocity. Such schemes are said to be *stochastic*. Eswaran and Pope (1988) proposed the use of random processes to drive the evolution of the turbulence field. The advantage of this approach comes in application to multiphase flows, wherein a source of instability is removed that arises from the forcing's dependence upon the velocity field; Chouippe and Uhlmann (2015) were able to demonstrate the robustness of this turbulence forcing approach in the context of an immersed boundary framework. Another distinct advantage of this approach is that it is clear what alterations to the (sufficiently time-averaged) fluid quantities were a result of the introduction of the particle-phase, since there is no interaction with the forcing scheme.

In the present simulations, the 'turbulence' properties were chosen such that fluid forces representative of those seen in the aforementioned nuclear systems were imparted on the particles, which was achieved through controlling the mean velocity fluctuation of the fluid. As a result of this process, the Taylor–Reynolds number of the present system was very low, $Re_\lambda = 2.5$. Given that this number was so low, and there was not the same scale separation present in the periodic boxes as would be seen in classical turbulent systems, the flow is characterised as 'chaotic', rather than turbulent. The methodology described in the present paper has the capability to generate much higher Taylor–Reynolds numbers and to resolve a fully turbulent flow if desired, which will be presented in future work looking at more generalised flow conditions. For now, the chaotic flow field gives a useful analogue, highlighting how agglomerating particle pairs in turbulent systems respond to dynamic perturbations to their velocities and configurations as they move through a stochastic velocity field.

The present study combines many of the described elements to offer a high-fidelity simulation approach that can facilitate fundamental knowledge generation on non-spherical particle interactions and agglomeration events. That is, a second-order accurate immersed boundary framework for the particle-phase, coupled to both a non-spherical hard-sphere collision algorithm as well as an adapted DLVO interaction potential accounting for the non-sphericity of the particles through local surface curvature. In addition, the Eulerian field is a stochastically forced chaotic box of fluid whose solution is computed through a seventh-order spectral element method, giving accurate resolution of the finest flow scales. The development of this direct numerical simulation-immersed boundary method

simulation framework offers the chance to learn about the intricate dynamics and interaction behaviours beginning just above the nanoscale. Beyond purely scientific insight, the work also aims to aid the nuclear industry where non-spherical particle interactions at the micron scale are frequently encountered.

2 Methodology

2.1 Fluid-Phase

The solution of the fluid-phase is computed through direct numerical simulation of the incompressible Navier–Stokes equations using the spectral element method. For this, we employ the open-source flow solver Nek5000 (Fischer et al. 2008), chosen for its scalability which facilitates parallel computations using a message passing interface approach.

The small $1mm$ cubic simulation domain encloses 20^3 evenly-distributed elements discretised into the Lagrange interpolants to seventh-order Legendre polynomials constructed on Gauss–Lobatto-Legendre nodes, totalling 2.7 million equivalent grid points. Thus, an exceptional level of fidelity is achieved in the fluid-phase for which all length scales of the flow field are resolved. The form of the solved Navier–Stokes equations is:

$$\frac{\partial \boldsymbol{u}}{\partial t} + \boldsymbol{u} \cdot \nabla \boldsymbol{u} = -\frac{1}{\rho}\nabla p + \nu \nabla \cdot \left[\left(\nabla \boldsymbol{u} + \nabla \boldsymbol{u}^T\right)\right] + \boldsymbol{f}_{EP}, \tag{1}$$

$$\nabla \cdot \boldsymbol{u} = 0, \tag{2}$$

where, $\boldsymbol{u}$, p, ρ, and ν are the instantaneous fluid velocity vector, pressure, density and kinematic viscosity, respectively. A forcing source term $\boldsymbol{f}_{EP}$ is introduced to the equations to maintain homogeneous and isotropic flow fluctuations according to the methodology of Eswaran and Pope (1988); in particular, we have followed the description given by Chouippe and Uhlmann (2015) for the implementation of our Fourier transforms. The fluid-phase parameters are chosen to be those of water at 20 °C for all of the discussed simulations. The simulation domain has periodic boundary conditions enforced in all three directions.

The stochastic forcing function generates a forcing field $\boldsymbol{f}_{EP}$ at each timestep, correlated in time, that is used to drive the evolution of the fluid field. As described, this is technically a turbulence forcing scheme, but presently it is used as a means of generating a chaotic flow field. Later simulations will look to increase the Taylor–Reynolds number and thus resolve classical turbulence. Six independent Uhlenbeck-Ornstein random processes are used to generate this forcing independently of the computed velocity field, corresponding to a real and imaginary part for each component of the wavenumber vector $\boldsymbol{\kappa} = \left(\kappa_1, \kappa_2, \kappa_3\right)$. As this computation does not rely on the resolved velocity field, this makes the chosen method suitable for our particle-laden flow, since the forcing scheme will not try to compensate for energy dissipated or gained as a result of the particle-phase.

To avoid the large data storage associated with importing a large precalculated forcing field for each timestep, this calculation is computed in situ with the fluid calculation. This is performed in Fourier-space and, as such, the full forcing field in Fourier-space is calculated on the first processor at the beginning of a timestep and passed to the others to be evaluated locally on the Cartesian grid points handled by the given processor through an inverse Fourier transform. In this forcing method, only small wavenumbers, corresponding

to the largest motions of the flow, are excited. Wavenumbers below a cut-off wavenumber receive no forcing contribution, i.e. $|\boldsymbol{\kappa}| \leq \kappa_{cut}$, chosen to be 2.3 times the smallest wavenumber, in line with Chouippe and Uhlmann (2015).

The forcing is parameterised a priori such that the flow field converges upon a desired Taylor–Reynolds number. Reliable relations are available to specify this parameterisation for a non-dimensional box of turbulence (Eswaran and Pope 1988; Chouippe and Uhlmann 2015), but not for a dimensional box of chaotic flow. The desired properties were therefore converged upon through alteration of the user-specified forcing parameters, whilst monitoring the outcome of a simulation. These forcing parameters are the forcing timescale (T_L) and the non-dimensional 'dissipation' parameter (ϵ^*), which were ultimately fixed as 0.01 s and 0.1, respectively.

The Uhlenbeck-Ornstein random processes $\widehat{\boldsymbol{b}}(\boldsymbol{\kappa}, t)$ are numerically updated using a finite-difference equation:

$$\widehat{b}_i^{j+1} = \widehat{b}_i^j \left(1 - \frac{\Delta t}{T_L}\right) + e_i^j \left(2\sigma^2 \frac{\Delta t}{T_L}\right)^{\frac{1}{2}}, \tag{3}$$

where the subscript i refers to the wavenumber direction, superscript j refers to the time level, and Δt denotes the fluid timestep. The variance of the process σ^2 is constructed from the two forcing parameters, $\epsilon^* = \sigma^2 T_L$. In the limit that $T_L \to 0$, the simulation becomes white noise (Eswaran and Pope 1988) and the mean energy input trivially tends to zero (Chouippe and Uhlmann 2015). As such, T_L and ϵ^* must be chosen independently in the forcing. The variable $e_i(\boldsymbol{\kappa}, t)$ is a complex random number that follows a standard normal distribution, generated using the Box-Muller transform approach.

The continuity condition in Fourier-space is $\widehat{\boldsymbol{f}}_{EP}(\boldsymbol{\kappa}, t) \cdot \boldsymbol{\kappa} = 0$, which is satisfied by:

$$\widehat{\boldsymbol{f}}_{EP}(\boldsymbol{\kappa}, t) = \widehat{\boldsymbol{b}}(\boldsymbol{\kappa}, t) - \boldsymbol{\kappa}(\boldsymbol{\kappa} \cdot \widehat{\boldsymbol{b}}(\boldsymbol{\kappa}, t))/(\boldsymbol{\kappa} \cdot \boldsymbol{\kappa}), \tag{4}$$

representing a projection of $\widehat{\boldsymbol{b}}$ onto the plane normal to $\boldsymbol{\kappa}$. Then, as described, an inverse Fourier transform is performed to obtain the entire forcing field $\boldsymbol{f}_{EP}$ used in the solution of the Navier–Stokes equations. Each random process exhibits a mean of zero in the limit $\Delta t \to 0$. The implication for the forced velocity field is that it also exhibits zero mean, as required by HIT. Secondly, each realisation of the forcing field is correlated in time since the stochastic process itself is correlated. These properties are laid out in Eqs. (5) and (6), respectively:

$$\langle \boldsymbol{b}(\boldsymbol{\kappa}, t) \rangle = 0, \tag{5}$$

$$\langle b_i(\boldsymbol{\kappa}, t) b_j(\boldsymbol{\kappa}, t+s) \rangle = 2\sigma^2 \delta_{ij} \exp(-s/T_L). \tag{6}$$

2.2 Particle-Phase

2.2.1 Non-spherical Morphology

Icospherical meshes comprised of 320 triangular faces are generated in the three-dimensional modelling software tool, Blender (blender.org). The relative lengths of the icosphere's principal axes are altered to create ellipsoids of two new morphologies. The morphologies, demonstrated in Fig. 1, are chosen to have a disk and needle shape of aspect ratio 5:1. This is

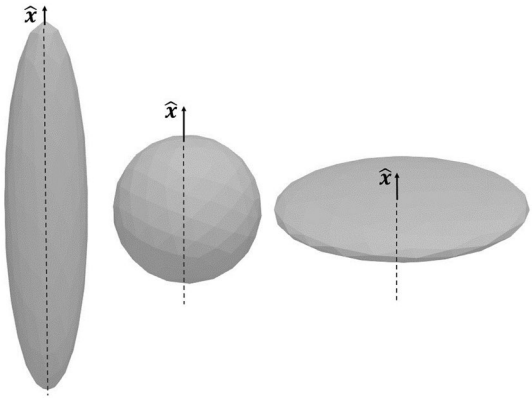

Fig. 1 Icospherical particle meshes of a needle, sphere and disk. Symmetry axis unit vectors are shown

achieved by scaling a sphere in the direction of the particle's x-axis, before scaling the other two axes' lengths accordingly such that volume is kept constant. This allows for the characteristic length $r = 50\mu m$, the volume-equivalent spherical radius, to remain representative of all morphologies used.

The particles created are spheroids, where two principal axes of an ellipsoid are of the same length. The term 'symmetry axis' will refer herein to that which is aligned with the x-direction in the body frame. There is circular symmetry about the x-axis for all three morphologies. Then, the asymmetric axes for the spheroids are those aligned with the y- and z-directions, about which there is geometric anisotropy. These asymmetries ultimately give rise to the orientational dependencies of the interparticle forces discussed later.

The particles' orientational states are vital to the calculations herein and must be tracked with accuracy. The chosen approach in the present work is to use a quaternion framework for fast and accurate rotations of the particle meshes.

2.2.2 The Immersed Boundary Method

An immersed boundary method is utilised to couple the particle-phase to the fluid following the method outlined by Mark and van Wachem (2008). A boundary condition matching the fluid velocity to the local particle velocity at its surface ensures the no-slip condition is satisfied. This is achieved by a ghost-cell mirroring technique, in which fluid 'ghost nodes' inside the particle boundary are manually set to values which ensure the requisite boundary condition. This requires a number of fluid points for each triangular face of the particle mesh. Inside the boundary are the ghost nodes; these are points in the fluid mesh that lie directly adjacent to the boundary. The location of each 'exterior point' is then determined from its respective ghost node. This is done by reflecting the ghost node across the particle face, such that the midpoint of the line formed between these two nodes represents a point directly on the particle surface. Typically, this process will not align the exterior point with a point also in the fluid mesh and so the exact velocity value at this point must be determined through spectral interpolation of the nearby fluid points, to determine its precise value.

Then, the no-slip condition is enforced by:

$$\boldsymbol{u}_G = 2\boldsymbol{u}_{IB} - \boldsymbol{u}_E, \tag{7}$$

with $\boldsymbol{u}_G$ the fluid velocity of the ghost node, $\boldsymbol{u}_{IB}$ the fluid velocity at the surface of the immersed boundary and $\boldsymbol{u}_E$ the fluid velocity of the exterior point. Finally, there are 'interior nodes' that lie inside the particle boundary but do not lie adjacent to the surface – these points are set to match the velocity at the nearest boundary.

Advection of the particles is computed by considering the joint contribution of the local viscous and pressure forces acting at the particle's surface. As the particle mesh topology does not necessarily align with that of the fluid mesh, interpolation is again employed, using the fluid pressure and viscous stress tensor. The total translational force experienced by the particle due to hydrodynamic forces is found by integrating these contributions over the surface S of the particle,

$$\boldsymbol{F} = \int_{IB} (-p\boldsymbol{n} + \boldsymbol{\tau} \cdot \boldsymbol{n}) dS, \tag{8}$$

With p the interpolated pressure and $\boldsymbol{\tau}$ the interpolated viscous stress tensor. In practice, this is computed through a sum across all faces of the icospherical mesh. Then, the torque $\boldsymbol{T}$ can be calculated by taking the cross-product in Eq. (10). This is evaluated numerically across the 320 faces through summations:

$$\boldsymbol{F} = \sum\nolimits_N (-p_f \boldsymbol{n}_f A_f + \boldsymbol{\tau} \cdot \boldsymbol{n}_f A_f), \tag{9}$$

$$\boldsymbol{T} = \sum\nolimits_N \boldsymbol{r}_f \times \boldsymbol{F}_f, \tag{10}$$

where the subscript f represents a quantity evaluated at a given face, N is the total number of faces, $\boldsymbol{n}$ is the face unit normal, and A_f is the area of the face. In Eq. (10), $\boldsymbol{r}_f$ is the vector pointing from the particle centre to the face centre.

The total torque of the body is used to update the angular velocity of the particle according to Euler's rotation equations in the particle reference frame, as a rigid-body is assumed:

$$\begin{aligned} I_x \frac{\mathrm{d}\omega_x}{\mathrm{d}t} &= T_x + \omega_y \omega_z \left(I_y - I_z\right), \\ I_y \frac{\mathrm{d}\omega_y}{\mathrm{d}t} &= T_y + \omega_x \omega_z (I_z - I_x), \\ I_z \frac{\mathrm{d}\omega_z}{\mathrm{d}t} &= T_z + \omega_x \omega_y (I_x - I_y), \end{aligned} \tag{11}$$

where $\boldsymbol{\omega} = (\omega_x, \omega_y, \omega_z)$ is the particle's angular velocity and $\boldsymbol{I}$ its inertia tensor, given for a general ellipsoid in the body-frame by:

$$\boldsymbol{I} = \begin{pmatrix} I_x & 0 & 0 \\ 0 & I_y & 0 \\ 0 & 0 & I_z \end{pmatrix} = \frac{m}{5} \begin{pmatrix} b^2 + c^2 & 0 & 0 \\ 0 & a^2 + c^2 & 0 \\ 0 & 0 & a^2 + b^2 \end{pmatrix}, \tag{12}$$

where m is the mass of the particle and a, b, c are the radii of the unrotated spheroid in the local x, y, z directions, respectively, with $b = c$.

2.2.3 DLVO Forces

The DLVO forces facilitate agglomeration, however when modelled explicitly they are only important at a length-scale much shorter than the radii of the particles. This creates a challenge in terms of capturing all relevant length scales in the simulation and underscores why typical modelling approaches opt for a macroscale model. In this work, the particle number is two and the simulation domain is small in order to include and study the full DLVO effects.

Due to their very short-range nature, most of the contribution to the DLVO force occurs in the vicinity of the point of closest approach between the two particle surfaces, and different relative orientations lead to different geometric properties at this point. It is this local geometric nature that is important to capture, to scale the magnitude of the interaction force correctly, since the forces themselves are a product of interacting surfaces.

Everaers and Ejtehadi (2003) proposed a term that accounts for the orientational dependency based upon the local surface curvature. In the present work, this term (Eq. 14) is applied as a dynamic scaling to the equations for two interacting spherical particles to give the following equation for the force between two interacting *spheroidal* particles. The first bracketed term on the right hand side of Eq. (13) is the well-known Hamaker (1937) expression representing the vdW attraction between homogeneously charged colloids, and the second term describes the EDL repulsion experienced by particles labelled i and j (Israelachvili 1992):

$$\boldsymbol{F}_{DLVO} = -\chi_{ij}\eta_{ij}\left(\frac{Ar}{12|\boldsymbol{d}|^2} - \frac{64\pi r n k_B T \Theta^2 e^{-\kappa|\boldsymbol{d}|}}{\kappa}\right)\hat{\boldsymbol{d}}, \tag{13}$$

$$\chi_{ij}\eta_{ij} = \frac{2\sigma^{-1}}{\sqrt{\left(\frac{1}{R_i} - \frac{1}{R_i'}\right)\left(\frac{1}{R_j} - \frac{1}{R_j'}\right)\sin^2(\alpha) + \left(\frac{1}{R_i} + \frac{1}{R_j}\right)\left(\frac{1}{R_i'} + \frac{1}{R_j'}\right)}}, \tag{14}$$

where $\boldsymbol{d}$ is the vector of closest approach, A is the Hamaker constant, r is the spherical radius, n is the number density of electrolyte ions, Θ is the reduced surface potential, k_B is the Boltzmann constant, T is the fluid temperature and κ is the inverse Debye length. The parameter σ is the characteristic length-scale of the particle, taken to be r; then, $R_{p=i,j}$ and $R'_{p=i,j}$ are the surface's principal curvatures at the point of closest approach and α is the relative orientation of the particles about the shared closest approach vector. A full description and derivation of this term is given by Schiller et al. (2011). The effect of $\chi_{ij}\eta_{ij}$ on the potential is that the well deepens for particles experiencing greater surface interaction as a result of their configuration.

The force arising from this interaction is evaluated at every timestep between particle pairs and is included in the particle's force balance, which also contains the fluid forces; then, the advection step is updated using the Euler integration scheme, suitable due to the very small timesteps used in the calculations. The charge distribution is assumed to be uniform across the particle surface, in line with the assumptions made in Hamaker theory (Hamaker 1937).

Finally, due to the divergent nature of the Hamaker expression in Eq. (13), as the separation tends to zero a cut-off distance must be chosen for the van der Waals force

beyond which the computed force does not increase. In this work the parameter is set to be 5 nm. This is a purely computational parameter to avoid divergence in the simulations.

2.2.4 Collisional Forces

Non-spherical hard-sphere collisions are computed through an adaptation of the common normal method presented by Jain et al. (2019). An iterative procedure seeks locations on the particle surfaces for which there is a shared normal vector that is also tangential to the surfaces. This is where the distance between two spheroidal surfaces is minimal; hence, this provides a means to obtain the closest distance vector between the surfaces, which is crucial in the calculation of the DLVO forces, as well as in the identification of a collision.

The chosen hard-sphere collision model does not permit overlap and so a distance greater than zero must be selected for identification of a collision: once inter-particle separation goes below this value a collision is deemed to have occurred. In this work, we have set a dynamic value for this parameter with magnitude based on the relative velocity of the particles at the points of nearest approach, an approach found to be well-suited to agglomeration modelling. This is because repeated particle collisions reduce the relative velocities of the particles, whilst the agglomeration process facilitates continual collisions as the particles are accelerated towards one another. The increasingly lower overall velocity state means that particles can become ever closer before the next collision needs to be implemented. Thus, more frequent sampling of large values of the van der Waals force is facilitated, without having to set prohibitively low time-steps to achieve the same result, as is the case with a static collision detection distance.

Once contact is determined, the collision forces $\boldsymbol{f}_c$ can be computed according to a further adaptation of Jain et al. (2019). Their non-spherical hard-sphere collision model is simplified here and applied to the particles.

The impulsive collision force is applied only at one timestep and acts over the time interval Δt. Calculations to determine the force $\boldsymbol{f}_c$ are made at the point of contact and variables computed at this contact point are denoted by the subscript c, whereas global variables that hold information of the full body are denoted by a subscript p.

At the moment prior to collision, the velocity at the contact point is

$$\boldsymbol{u}_c = \boldsymbol{u}_p + \boldsymbol{\omega}_p \times \boldsymbol{r}_c, \tag{15}$$

where $\boldsymbol{r}_c$ is the vector joining the contact point and the particle centre. At time level n, the quantity $\boldsymbol{u}_c$ is given by

$$\boldsymbol{u}_c^n = \boldsymbol{u}_c^{n-1} + \mathbf{K} \cdot \boldsymbol{p}_c, \tag{16}$$

where $\boldsymbol{p}_c$ is the linear momentum. The derivation of this can be found in the cited paper. This can then be used to derive the force via

$$\boldsymbol{f}_c = m \frac{\boldsymbol{u}_c^n - \boldsymbol{u}_c^{n-1}}{\Delta t} \tag{17}$$

where m is the mass of the particle. This could be applied to our particle mesh and hence directly included in the force balance. However, our approach differs. Since we have a rigid body, the angular velocity is defined globally, allowing us to derive the particle angular velocity from

$$\boldsymbol{\omega}_p = \boldsymbol{\omega}_c = \frac{\boldsymbol{r}_c \times \boldsymbol{u}_c}{|\boldsymbol{r}_c|^2} \tag{18}$$

which we then use to update our particle velocities by rearranging Eq. (15),

$$\boldsymbol{u}_p = \boldsymbol{u}_c - \boldsymbol{\omega}_p \times \boldsymbol{r}_c. \tag{19}$$

In Eq. (16) the symmetric system matrix is given by

$$\mathbf{K} = m^{-1}\mathbb{I} + [\boldsymbol{r}_c]_\times^{\mathrm{T}} \cdot \mathbf{i}^{-1} \cdot [\boldsymbol{r}_c]_\times \tag{20}$$

where $[\boldsymbol{r}_c]_\times$ is the skew symmetric matrix of $\boldsymbol{r}_c$ and $\mathbf{i}$ is the inertia matrix in the global coordinate system arising from the transformation $\mathbf{i} = \boldsymbol{A} \cdot \boldsymbol{I} \cdot \boldsymbol{A}^{\mathrm{T}}$ with $\boldsymbol{I}$ being the body frame inertia tensor defined in Eq. (12). The inverse of the particle mass multiplies the identity matrix.

Using Newton's third law to share the linear momentum, we arrive at the following equations:

$$\boldsymbol{u}_{c,1}^n = \boldsymbol{u}_{c,1}^{n-1} - \mathbf{K}_1 \cdot \mathbf{p}_c, \tag{21}$$

$$\boldsymbol{u}_{c,2}^n = \boldsymbol{u}_{c,2}^{n-1} + \mathbf{K}_2 \cdot \mathbf{p}_c. \tag{22}$$

Taking the difference of these two equations gives the relation

$$\mathbf{p}_c = -\mathbf{K}_{12}^{-1} \cdot \Delta\boldsymbol{u}, \tag{23}$$

with $\mathbf{K}_{12} = \mathbf{K}_1 + \mathbf{K}_2$.

By defining the relative velocity between the two particles at the point of collision as $\boldsymbol{u}_r$, we can in turn define the change in relative velocity due to a collision $\Delta\boldsymbol{u} = \boldsymbol{u}_r^{n-1} - \boldsymbol{u}_r^n$ in a way that can be implemented using known quantities

$$\Delta\boldsymbol{u} = \boldsymbol{u}_r^{n-1} + e(\boldsymbol{u}_r^{n-1} \cdot \mathbf{n})\mathbf{n}, \tag{24}$$

where the second term on the RHS of Eq. (24) is a closure coming from the *Poisson hypothesis* (Jain et al. 2019) and e is the normal coefficient of restitution.

The cited paper also provides a lubrication model whose magnitude is scaled by the local curvature, similarly to the present DLVO implementation. In the present work, lubrication forces were omitted because the van der Waals forces were found to be dominant in the present system at the relevant separations. This was confirmed through a mesh-sensitivity analysis wherein dramatically increasing the fluid-phase resolution, such that the interstitial fluid was better resolved, was seen to have no influence over close-range particle motion.

The particles receive a force from the fluid in their advection, they exert an implicit force on the fluid through their boundary, and they interact with one another through collisions and inter-particle forces. In this way, the multiphase system is *four-way coupled*.

Table 1 Calcite particle parameters used in the simulations

Parameter	Value	Units
Particle density, ρ_p	2710	kgm^{-3}
Volume-equivalent spherical radius, r	50	μ m
Restitution coefficient, e	0.4	–
Hamaker constant, A	22.3	zJ
Inverse Debye length, κ	328,947,368	m^{-1}
Surface charge density, Θ	0.00037	Cm^{-2}
Initial particle relative velocity, $u_{p,0}$	0.875, 4.20	mms^{-1}
Van der Waals cut-off distance	5	nm
Stokes number St (based on root-mean-square of velocity fluctuations and box height)	0.013	–

Table 2 Fluid parameters used in the quiescent and turbulent simulations

Parameter	Value	Units
Density, ρ	997	kgm^{-3}
Kinematic viscosity, ν	10^{-6}	Pa · s
Taylor Reynolds no., Re_λ	0, 2.5	–
Mean velocity fluctuation	0, 0.0077	ms^{-1}
Domain length	1	mm
Temperature	293	K
Timestep, Δt	2×10^{-7}	s

3 Results and Discussion

The aim of the investigation was to generate insight into the agglomeration behaviour of non-spherical particles in a fluid. The chosen numerical experiments are designed to isolate the roles of morphology, orientation and of the background flow as best as possible in this highly complex system. The investigation also demonstrates the robustness of the method.

3.1 Non-spherical Agglomeration Dynamics in a Quiescent Fluid

To assess the influence of morphology and orientation, free from the impact of a fluctuating flow field, and to generate a base-case for comparison to the subsequent chaotic results, an investigation was conducted in a quiescent liquid (water at 20 °C). The particle parameters were chosen to match calcite, which is often used as a nuclear waste simulant due to its similar characteristics to nuclear waste materials. A full description of these parameters is presented in Table 1. Additionally, Table 2 presents the fluid parameters used in both the quiescent and chaotic simulations described later.

Two non-spherical particles of the same morphology were injected into the box of fluid with a fixed surface separation distance of 5μm. This distance is one tenth of the characteristic radius of the particles but since the fluid is having minimal effect on the motion of the particles in the quiescent case during approach, and since the DLVO

forces do not become important until the separation distance is below the order of 1μm, this was deemed to be a sensible initial distance to save computational resources. Upon injection, the closest approach vector between the two particles was calculated and it was along this direction they approached, with a relative velocity of $0.875\, mms^{-1}$ chosen as a representative value in accordance with observations of relative collision velocities made in a $Re_\tau = 180$ channel flow (Mortimer et al. 2020). The simulations were allowed to run for an equal amount of time pre- and post-collision such that the full interaction behaviour could be simulated. This is important, since it was found that agglomeration does not happen instantaneously under this model; rather, kinetic energy is lost in successive collisions as per the interplay between the hard-sphere model and the DLVO forces. Specifically, the attractive vdW force acts to bring the two particles back together after a collision, and in each instantaneous collision the particle pair retain only 40% of their pre-collision velocity. This allows two particles to become trapped in the potential well in a quasi-equilibrium state.

Taking a Monte Carlo approach, the orientations of both non-spherical particles were randomised across all three rotational degrees of freedom (i.e. the Euler angles). This requires the use of a special distribution in order to achieve uniform sampling on the unit sphere (Janin et al. 2021), used here for particle orientation. The distributions of these angles were monitored to determine when a representative sample had been taken of the full orientational parameter space. Once this was achieved, after 120 simulations per morphology, probability density functions (PDFs) of separation distance and relative velocity were generated to compare the morphologies' behaviour.

From Fig. 2, it can be observed that the needles have a greater propensity to agglomerate across the orientational parameter space for our chosen initial velocity. This is evidenced by the needles remaining closer together, with lower relative velocity on average. The rightmost PDF shows a sharp peak at the prescribed initial velocity, as would be expected, but the interesting behaviour occurs on the left of the plot where we see the post-collision behaviour accumulating. We can see from the variation in Fig. 2 that the vdW force acts to alter the observed coefficient of restitution: particles that rebound are still decelerated and as such lose additional energy in the interaction. The fact that orientation alters the strength of this force gives rise to the variance. There is a wider variation in the behaviour of the disks which can be partly attributed to fewer agglomeration events (events for which there is an oversampling of very low relative velocities).

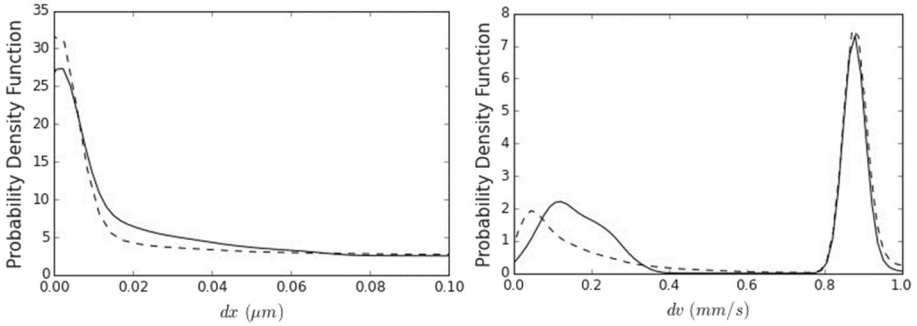

Fig. 2 PDFs of inter-particle separation (left) and relative particle velocity (right) compared for the two morphologies. *Solid line* (–) represents *disks* and *dashed* (- -) represents needles

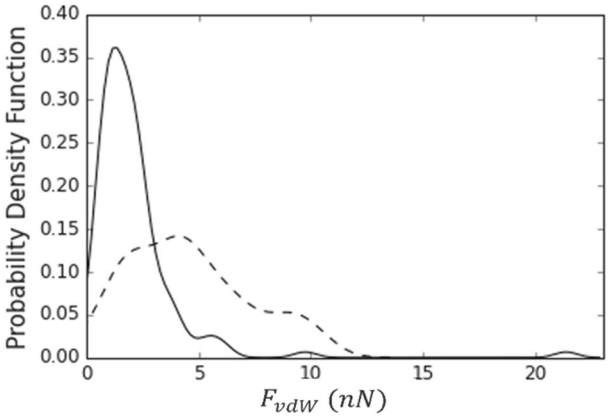

Fig. 3 PDFs generated using the maximum van der Waals force magnitude F_{vdW} achieved in each simulation. *Solid line* (–) represents *disks* and *dashed* (- -) represents needles

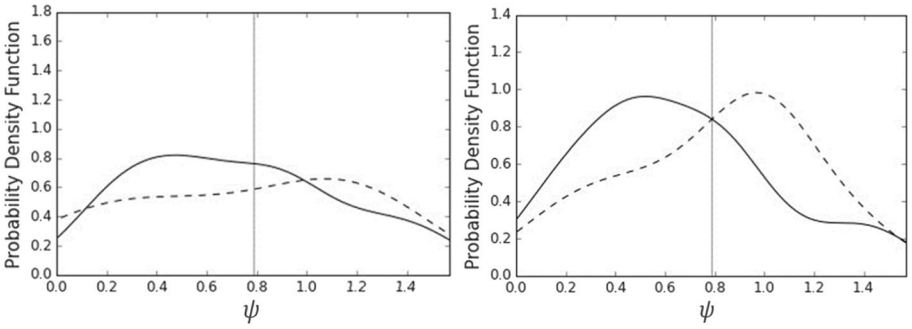

Fig. 4 PDFs of the relative orientation of symmetry axes ψ for needles (left) and disks (right). *Solid line* (–) represents data gathered from simulations with agglomeration, and the *dashed line* (- -) represents bouncing simulations. The *vertical line* indicates a value of $\frac{\pi}{4}$

An interrogation of the vdW forces indicates that disks resolve both the highest and lowest individual attractive force at the point of collision but the needles overall have much higher average values of the vdW force across orientations. This helps to explain why 73 disks agglomerated and 47 rebounded, at a rate of 61%, whilst 105 needles agglomerated and just 15 rebounded, at a rate of 88%. The disks formed the strongest agglomerates of the two morphologies when a face-face interaction occurred, but this was rare, as evidenced by the small spike in the distribution on the right of Fig. 3. The surface area of the disks is greater than the needles at a fixed volume, and so these results run contrary to what may be an initial expectation. This suggests that the way that the shape's curvature is distributed across the face, which is different for the two morphologies, must play a role in agglomeration propensity when conducting a study across the full orientational parameter space. Further investigation is required to understand the precise geometrical mechanism that leads to this difference. To begin to elucidate this further, the computed collisions were subcategorised into agglomeration and rebound events, and the relative orientations of the particle symmetry axes were assessed. For reference, the unit vectors indicating these symmetry axes were included in Fig. 1. The results of this division can be seen in Fig. 4.

We observe that for both needles (left) and disks (right), there is a clear dependency on the relative orientation of the particle symmetry axes when it comes to determining

whether particles agglomerated. Parallel configurations appear to be favoured, which is in line with the results of Schiller et al. (2011) who studied attractive spheroidal particles, without consideration of any dynamic fluid effects. The alignment phenomenon occurs partly because alignment of the symmetry axes facilitates greater surface interaction and hence allows the maximal attractive vdW forces to be experienced: the case of a maximally attractive configuration requires exact alignment. However, the PDFs do not peak at this value, and there is still a crossover in the two distributions, because there are more orientational degrees of freedom at play.

The disks have the strongest dependency on this parameter, with a much starker contrast between the two distributions. One explanation for this is that the disks require near-parallel alignment of their symmetry axes in order to facilitate an interaction strength that permits agglomeration. Further, the particles may experience different collision points on the surface with different frequencies under uniformly random distributions of their initial orientations. More investigation is required again to understand why this would be the case, but it must arise due to a geometric effect. It is evident however that the morphology affects the DLVO interaction in a way that favours attraction between needles rather than disks. As alluded to, the variables most pertinent to the agglomeration outcome are the points of closest approach on the respective surfaces as the particles approach one another and then again as they separate post-collision. It is these local points that are fed into the DLVO model to determine curvature at the point of closest approach and thus the interaction strength. We can simplify the assessment of this variable without losing much information by isolating the points that are struck during the collision on the respective surfaces. The following results use the parametric form of the ellipsoidal equation, wherein the unrotated ellipsoid is parameterised in terms of two angles, $0 < \theta < \pi$ and $-\pi < \phi < \pi$, which define a unique location on the surface. For a spheroid whose symmetry axis is in the x' direction, varying θ for constant ϕ defines the *parallels* of the surface, whilst varying ϕ and keeping θ constant defines the *meridians* of the surface; these are the *lines of curvature*. Traversing a parallel of the surface retains the same curvature, since these lines represent the circular symmetry about the so-called symmetry axis. Whereas traversing the meridians will lead to a variation in the local surface curvature, since they are of elliptical shape, with such a

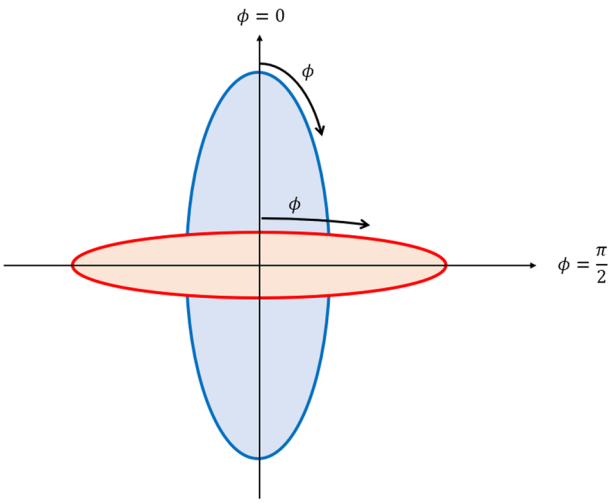

Fig. 5 Meridian of the surface, describing the angle ϕ, for disks (*red*) and needles (*blue*)

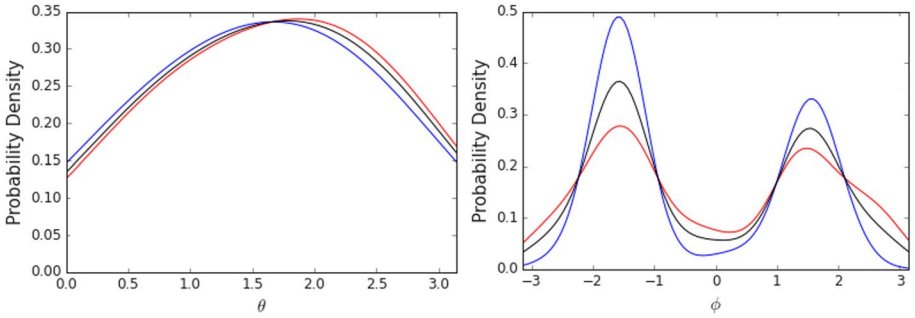

Fig. 6 PDFs of collision points in terms of the parametric angles θ (left) and ϕ (right) for disks. The *red line* (–) represents simulations with agglomeration events, the *blue line* (–) represents the bouncing events and the *black line* (–) represents the combined distribution

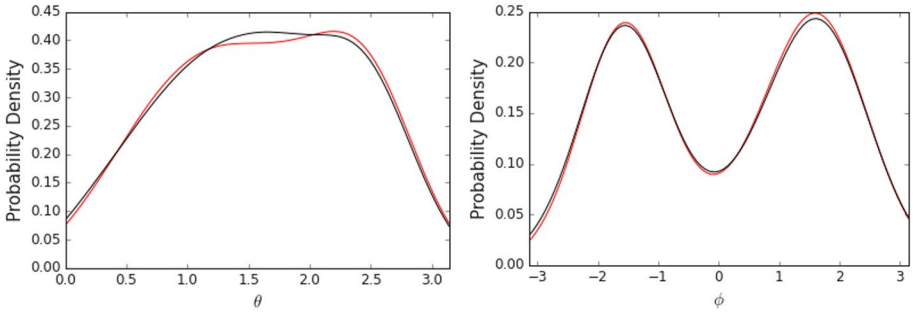

Fig. 7 PDFs of collision points in terms of the parametric angles θ (left) and ϕ (right) for needles. The *red line* (–) represents simulations with agglomeration events, and the *black line* (–) represents the combined distribution of bounced and agglomerated. The bounced distribution is omitted due to sample size

cross-section drawn in Fig. 5. In theory, agglomeration outcomes and interaction strengths ought to be a function of ϕ alone when considering the collision points on the surface due to the particles' circular symmetry. The results of this analysis are presented above in Figs. 6 and 7.

The results agree with the prediction made in the previous paragraph; that is, there is no clear dependence on θ, with the small deviation between lines probably being attributable to sample size. Whereas a very significant trend is observed for ϕ. In particular, in Fig. 6, the total collision points on the surface of the disk are collecting at around $\phi = \pm\frac{\pi}{2}$, which is the location of the edge points of the disks. At these locations, the DLVO forces induced are minimal since the surface interaction is minimal. As expected, then, at these locations there is a clear predominance of bouncing events, rather than agglomeration events. Conversely, near to the face of the disk, at around $\phi = 0$, where DLVO forces being induced are maximal, there is a predominance of agglomeration events.

The breakdown for needles, seen in Fig. 7, does not carry the same insight for agglomeration as it did with the disks, on account of the fact that there is not a great enough sample size of bouncing events to make any meaningful conclusions. The agglomeration distribution very closely follows the total distribution, as would be expected given the weighting of agglomeration events in the overall collision sample; however, a pattern is

perhaps emerging where there is an overrepresentation of agglomeration at $\phi = \pm\frac{\pi}{2}$, and a very slight underrepresentation at $\phi = 0$, which is the opposite of the disks. Further investigation is required to confirm this since this small difference could just as easily be attributed to noise.

Turning the focus to the total distributions of disk collisions and needle collisions, there is a clear difference in the locations on the surfaces that ultimately experience a collision, irrespective of DLVO forces. The probability of colliding at the various locations on the particle surfaces is different based on morphology, even when uniformly randomly sampling the orientations, as is the case here. This raises a question of why.

One hypothesis can be constructed by considering particle shape. Disks are shown to be much more likely to collide in the vicinity of the circular band that defines the 'edge' of the shape, and needles are much more likely to collide along their long edges, as opposed to their end points. Under a stretching transformation, the spheroids remain topologically equivalent, and the collision points accumulate in similar regions of the (θ, ϕ) parameter space. However, the physical mechanisms driving these accumulations differ due to the anisotropic geometry and curvature distributions of the spheroid. Specifically, collisions peak on the circular band with the greatest radius, or the central parallel line of curvature, (that lies normal to the local x axis at $x = 0$) for both spheroid types. In a disk morphology, this circle manifests itself as the so-called 'edge' of the shape – and in needles it is simply the central circle perpendicular to the so-called 'long-edge', where DLVO forces happen to be maximal.

Relating this back to Fig. 3, there were not many events where minimal forces were induced for the needles, nor maximal forces induced for the disks, which led to results contrary to initial expectation. A good explanation for this finding, therefore, is linked to the described effect. Since there are only two points on a needle where the forces are minimised, the end-points, or the poles, it stands to reason that these points are not often frequented in collisions over the entire orientational parameter space. This runs in contrast to disks, where the minimal forces are induced on the entire circular band, because curvature is maximal here. The maximal forces on the disks are only induced at two points: the direct centres of the faces, and the least frequented locations. This is in contrast to needles, where the maximal forces exist on the band around the centre of the shape, the most frequented locations.

3.2 Non-spherical Agglomeration Dynamics in a Turbulent Fluid

A statistically stationary periodic box of homogeneous and isotropic chaotic flow was simulated with properties chosen in line with those typically observed in nuclear waste processing systems (Mortimer et al. 2020). Both the Taylor–Reynolds number and the root-mean-square velocity fluctuation of the fluid were matched to values observed in the channel flow approximating this system, with the goal of imparting realistic fluid forces onto the particle surfaces, to influence the agglomeration process in an insightful way. The particles in this environment experience a chaotic fluid motion which influences agglomeration through particle trajectories and orientation changes. In particular, the flow was observed to dramatically change the relative orientations of the particles as the simulations progressed, leading to a change of the local surface curvature between particles which in turn dynamically alters the DLVO potential well depth and makes agglomeration either more or less likely. The resolved collision mechanics were also observed to have a significant influence, where an interesting interplay was seen between the non-spherical collision algorithm and

the attractive forces. Future studies will look to increase the Taylor–Reynolds number so as to better approximate classical turbulent situations in effort to uncover the dynamics of collisions in more turbulent regions (such as the buffer layer in a wall-bounded flow), but for the scope of the present study the desired effects were well modelled.

Pairs of disks and needles were injected into the box with randomised initial orientations. An example interaction event is displayed below in Fig. 8. The same converged fluid file was used to start each of the simulations, but the location of injection for the centre of the injected particle pair was random uniformly distributed throughout the box to ensure that a range of conditions were sampled. Further, the stochastic nature of the fluid forcing ensured that no two simulations evolved the same. The particles were injected into the box with a fixed inter-surface separation distance of 2 μm. This distance was chosen to ensure that a collision occurred, and that it was at the correct velocity, but also far enough apart to ensure the particles were outside of the effective range of the DLVO forces so that the full initial interaction was simulated. Initially placing the particles too far apart leads to much of the information of the initial conditions being lost in the chaos of the flow field by the time of a collision, if a collision still occurs at all: this is just the nature of having only two particles subject to a chaotic field and so it was decided that the collision velocity was the most important parameter to ensure and fix.

The particles were given an initial relative velocity of 0.0042 ms^{-1} which corresponds to the measured averaged collision velocity for colliding particles in the viscous sublayer of the complementary channel flow simulations (Mortimer et al. 2020). The chosen particle velocity also means that the results are not one-to-one comparable with the quiescent flow results, as the kinetic energy of the system is now higher but overall trends can be compared and contrasted. By choosing these system parameters, we enable later comparison with the channel flow study as well as a validation of our in-house LPT code and the assumptions therein.

The chemical parameters remained the same as for the quiescent box in Table 1. The interactions were allowed to run for a total simulated time of 3 ms, which is much longer than in the quiescent study. This was necessary to allow enough time for the flow to significantly influence the particle velocities or for an agglomerate to form, as described. Upon an off-centre or off-normal collision, non-spherical particles induce rotation, and so secondary

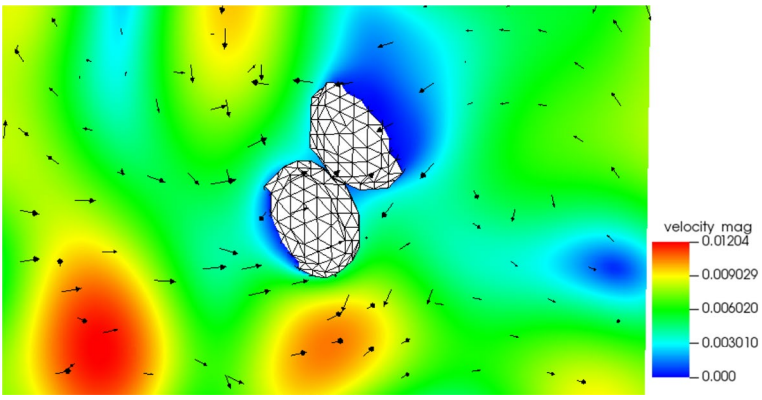

Fig. 8 Example of two interacting immersed boundary disks in a chaotic velocity field ($Re_\lambda = 2.5$) represented by a pseudocolour slice of the local velocity field. The *colour bar* indicates instantaneous velocity magnitude (ms^{-1}). The vectors indicate local flow direction

collisions are much more likely, as well as further interesting dynamics. Agglomeration can occur through the mechanism of particles remaining close by and rotating, hence it is necessary to capture behaviours like this that take more simulation time to resolve. If the particles do not lose enough kinetic energy through their first collision to agglomerate, then a secondary collision may allow this.

In Table 1, the relevant Stokes number is also reported. The particle response time was given by $\tau_p = \rho_p d^2/(18\rho_F \nu)$ for our particles with characteristic diameter $d = 100\mu m$, and fluid density $\rho_F = 997 kgm^{-3}$.

Figure 9 highlights three key cases of interacting disks in the chaotic box. Case 1 is an example of an agglomerate forming. The method through which this occurs is energy loss in successive collisions reducing the relative velocities of the particles enough such that they cannot escape the potential well by the final collision. In the second case, we observe the particles remaining close, but not due to an agglomeration event. Rather, the particles experience similar flow conditions due to being advected by the same eddy, and a small van der Waals contribution keeps them close before finally they are swept apart by an adverse velocity gradient, sharply increasing their separation. In the third case, a pair of disks collide on their edges and hence the van der Waals force is not strong enough to greatly influence the collision at the given velocities and so they move apart indefinitely.

The role of morphology on the behaviour of the system was assessed. Here, 80 needle simulations are presented in which 39 particle pairs agglomerated and 41 did not, at a rate of 49%. We present 64 disk simulations in which 9 agglomerated and 55 did not, at a rate of 14%. We also present 53 sphere simulations in which 20 agglomerated and 33 did not, at a rate of 37%. Analysis of these simulations led to the probability density functions of separation distance and relative velocity given in Fig. 10, which shows a comparison between the behaviours of spheres, needles and disks. Note that spheres were omitted from our initial study since there is no orientational dependency of their DLVO forces – the isolated variable under investigation there.

It can be seen that the overall variation of the PDFs is increased by the introduction of a chaotic field. The influence of attractive forces and agglomeration can be seen from the biasing of the PDFs towards low velocities and inter-surfacial separation distances. We determine from the means, indicated by the vertical lines, that there is a strong dependency on morphology. With the given system parameters, it is observed that needles have the strongest agglomeration favourability, followed by spheres and then by disks. From the

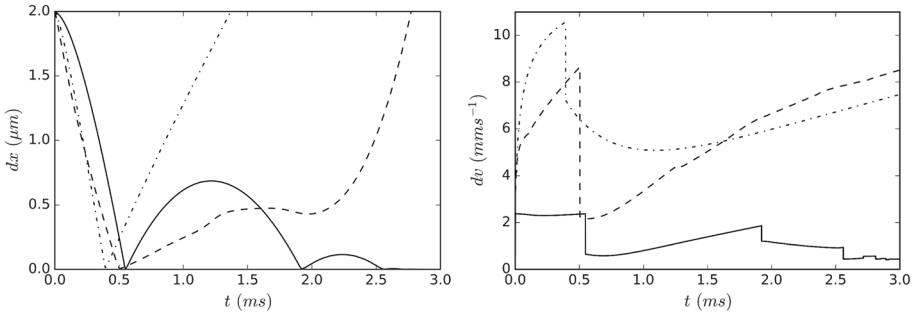

Fig. 9 Temporal evolution of separation distance and relative velocity of three illustrative interaction cases between disks. The *solid line* (–) is referred to as *case 1*, the *dashed line* (- -) as *case 2* and the *dotted line* (···) *case 3*

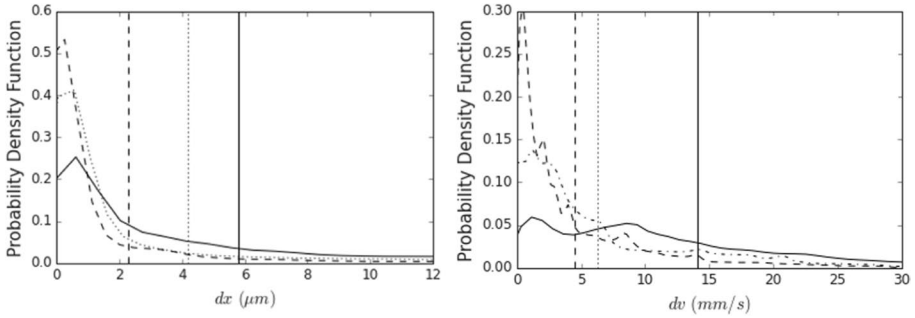

Fig. 10 PDFs of inter-particle separation (left) and relative particle velocity (right) compared for three morphologies in the chaotic flow box. *Solid line* (–) represents disks, *dashed line* (- -) represents needles and *dotted line* (···) represents spheres. The mean value is indicated by the associated vertical line

agglomeration statistics, the influence of chaotic flow appears to have widened the disparity between disks and needles further when compared to the quiescent case. Clearly, under these system parameters, it is unfavourable for disks to agglomerate. An interrogation of the maximum velocities experienced by each morphology provides insight into the cause: the disks are being accelerated by the flow field to a much greater extent than the other two morphologies which are comparable in terms of their acceleration. The disks are rising to velocities twice that of the needles in the most extreme cases. This is partly due to the increased surface area of the disks for the hydrodynamic forces to act on, hence drag on the disk is likely to be stronger. The result is that the kinetic energy of the disks is increased quickly to levels where agglomeration becomes unlikely, and the requirement for a maximally attractive configuration is increased.

To understand which orientations lead to agglomeration in the randomised flow field, and hence the kind of structures most likely to form, data was once again collected on the angles between the symmetry axes of disks and needles and compared in cases with and without agglomeration. It can be observed from Fig. 11 that the particle pairs which agglomerate tended to have their symmetry axes aligned for the needles, as was the case before. In comparison to the quiescent box, the influence of the chaotic field, and higher particle initial velocity, is that an alignment of the symmetry axes has become more

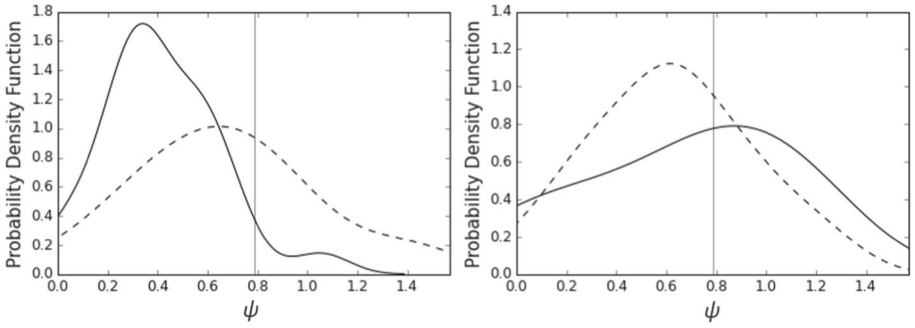

Fig. 11 PDFs of the relative orientation of symmetry axes ψ for needles (left) and disks (right) in the turbulent box compared for agglomerating (–) and rebounding (- -) particles. The *vertical line* indicates a value of $\frac{\pi}{4}$

pronounced in the case of agglomeration, meaning that there is a stronger requirement for such an alignment, in order for an agglomeration event to take place. For near-perpendicular configurations there is almost no agglomeration able to take place. Both distributions, that of the agglomerated particles and the rebounded ones, appear to have shifted towards lower relative orientations, indicating that there is a promotion of parallel alignment irrespective of agglomeration or rebound. This could be attributed to the vdW force's effect over time. It could also be due to the fact that the particles were injected close to one another: Voth and Soldati (2017) relay that the orientation of particles is strongly dependent upon the local velocity gradient tensor. Hence, two nearby particles experiencing similar local flow conditions are more likely to be aligned with one another. This effect could be helping to bias the alignment when moving to the second studied system.

Interestingly, the behaviour has reversed in the case of the disks. The particles that agglomerate are roughly evenly distributed across the parameter space, whilst the rebounding particles show a slight bias towards parallel alignment; however, the location of the peak of the 'bounced' distribution is similar to that of the needles. The 'agglomerated' distribution may be anomalous for the disks since so few particles agglomerated and hence the sample size is low. Since the disks were much more susceptible to the forces from the flow field, the local flow dominates the interaction to a greater extent, and it is more difficult to extract the DLVO effects in the analysis stage.

Repeating the analysis we conducted on the collision points, we see from Figs. 12 and 13 that the overall trends are retained, however the coherence is severely diminished. This is particularly the case for the needles where the peaks have remained in roughly the same position but the distributions appear to be convoluted, which is the influence of the fluctuating flow field. Interestingly, the disks retain the same behaviour in terms of their agglomeration distribution, even though that was not the case for their particle alignment. The disks show a very strong agglomeration dependence on $\phi \approx 0$ which matches the explanation given above. That is, disks require a face-to-face contact to facilitate a strong enough interaction to overcome the increased fluid effects they experience. Secondly, the total distribution of collision points has flattened to become a much more uniform distribution, which indicates that the flow in some way prevents disks from colliding on their edges, or promotes face-face collisions, much more than observed in quiescent conditions.

Finally, it was demonstrated in our simulations that the background flow field was not strong enough to break agglomerates; however, there is no reason this should not be

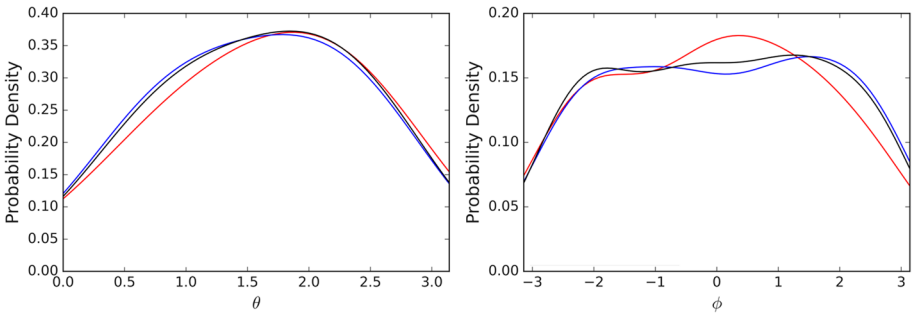

Fig. 12 PDFs of collision points in terms of the parametric angles θ (left) and ϕ (right) for disks in a chaotic flow. The *red line* (–) represents simulations with agglomeration events, the *blue line* (–) represents the bouncing events and the black line (–) represents the combined distribution

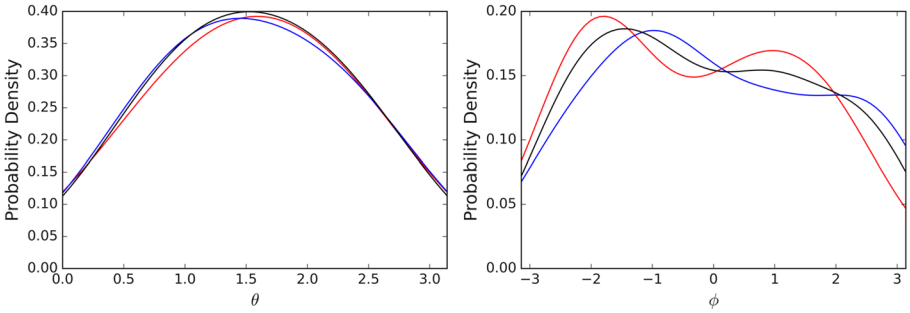

Fig. 13 PDFs of collision points in terms of the parametric angles θ (left) and ϕ (right) for needles in a chaotic flow. The *red line* (–) represents simulations with agglomeration events, the *blue line* (–) represents the bouncing events and the *black line* (–) represents the combined distribution

possible under our DLVO potential model. The fluid must supply enough energy to allow the particles to escape the potential well, but this is not realised at such a low Reynolds number. The inclusion of many particles is the next avenue for study, and a tertiary particle collision could also supply enough energy to break an agglomerate.

4 Conclusions

A methodology for structure-resolved simulation and analysis of non-spherical particle interactions has been demonstrated in both quiescent and chaotic systems. Direct numerical simulation and an adapted immersed boundary method, capable of modelling agglomeration of non-spherical particles in chaotic flows and in turbulence, has been used here to predict interactions between particles in a fluctuating flow field.

Analysis of collisions occurring in quiescent conditions indicates that needles are more likely to agglomerate for uniformly random initial orientations, when compared to volume-equivalent disks. Parallel configurations are also demonstrated to be favoured when considering the relative orientations of both morphologies.

Binary interactions of disks and needles in a fluctuating flow field representing typical values of a nuclear waste processing system have also been presented in demonstrative examples, where they have been analysed and the important features relating to agglomeration discussed. Resolution of non-spherical particle agglomeration has been achieved and it is shown that the non-sphericity of the particles generates strong anisotropy in the agglomeration behaviour. A great richness was seen in the interactions studied, as the chaotic flow altered the trajectories, kinetic energies, and relative orientations of the particles as the simulations progressed, leading to changing geometric characteristics at the points of closest approach and hence different DLVO magnitudes and agglomeration outcomes. It was demonstrated that needles and disks are more likely to agglomerate when their symmetry axes are aligned, such that their long axes are parallel to one another. However, particularly in the case of the disks, whose surface area is greater, the interacting flow begins to take precedence over particle configuration in determining interaction outcomes. In particular, the disks become accelerated to such velocities that agglomeration becomes energetically unfavourable to an extent that is not seen for the needles.

Lastly, the contact points of collision on the particle surfaces were analysed, with strong reliance on this parameter demonstrated in the results. Disks are seen to be much more likely to agglomerate when colliding with contact made between the centre of their faces, which is also the case for needles. However, needles were shown to retain agglomeration outcomes over a wider spread of this total parameter space when compared to disks.

Future work should aim to investigate further the relationship between the morphology of the particles and agglomeration, and in particular the distribution of surface curvature and how it influences the collision outcome. The asymmetry in the distributions of collision points between the two morphological cases, despite both having uniform randomly sampled orientations, is also an area under investigation. Increasing the Taylor–Reynolds number will allow a greater range of flow scales to be introduced to the system and as such will strongly influence the particle dynamics which will in turn affect agglomeration, it will be of interest to contrast such a system with this intermediate system to build further the picture of turbulent agglomeration as it relates to the local flow characteristics. Finally, multiple particles should be included into the simulations in order to understand the larger scale structures formed by the agglomeration process in turbulence and other emergent phenomena.

Acknowledgements This work was supported by Sellafield Ltd and the UK Engineering and Physical Sciences Research Council (EPSRC) through grant EP/L01615X/1 for the EPSRC Centre for Doctoral Training in Fluid Dynamics at Leeds and grant EP/S01019X/1 for project TRANSCEND (Transformative Science and Engineering for Nuclear Decommissioning).

Author's Contribution Concept, inception and strategy: MF, LFM, JPA. Model development: JPA, LFM, MF. Code development: JPA, LFM. Results and analysis: JPA, LFM, MF. First paper draft: JPA. Review: LFM, TNH, JP, MF. Project guidance: LFM, TNH, JP, MF.

Data Availability Data will be made available via UoL's repository.

Declarations

Conflict of interest The authors declare no competing interests.

References

Almohammed, N.: Modeling and Simulation of Particle Agglomeration, Droplet Coalescence and Particle-Wall Adhesion in Turbulent Multiphase Flows. PhD Thesis. Helmut Schmidt University (2018)

Alvelius, K.: Random forcing of three-dimensional homogeneous turbulence. Phys. Fluids **11**, 1880–1889 (1999)

Balachandar, S., Eaton, J.: Turbulent dispersed multiphase flow. Annu. Rev. Fluid Mech. **42**, 111–133 (2010)

Breuer, M., Almohammed, N.: Modeling and simulation of particle agglomeration in turbulent flows using a hard-sphere model with deterministic collision detection and enhanced structure models. Int. J. Multiph. Flow **73**, 171–206 (2015)

Chen, S., Li, S., Marshall, J.S.: Exponential scaling in early-stage agglomeration of adhesive particles in turbulence. Phys. Rev. Fluids **4**, 024304 (2019)
Chouippe, A., Uhlmann, M.: Forcing homogeneous turbulence in direct numerical simulation of particulate flow with interface resolution and gravity. Phys. Fluids **27**, 123301 (2015)
Derjaguin, B., Landau, L.: Theory of the stability of strongly charged lyophobic sols and of the adhesion of strongly charged particles in solutions of electrolytes. Acta Physicochim. **14**, 633–662 (1941)
Eaton, J., Fessler, J.: Preferential concentration of particles by turbulence. Int. J. Multiph. Flow **20**(Supplement 1), 169–209 (1994)
Elghobashi, S.E., Truesdell, G.C.: Direct simulation of particle dispersion in a decaying isotropic turbulence. In: Seventh Symp. on Turbulent Shear Flows, pp. 121–122 (1989)
Eswaran, V., Pope, S.: An examination of forcing in direct numerical simulations of turbulence. Comput. Fluids **16**, 257–278 (1988)
Everaers, R., Ejtehadi, M.R.: Interaction potentials for soft and hard ellipsoids. Phys. Rev. E **67**, 041710 (2003)
Fischer, P.L., Lottes, J.W., Kerkemeier, S.G.: Nek5000. Retrieved 01–08–2022, from http://nek5000.mcs.anl.gov (2008)
Fujita, M., Yamaguchi, Y.: Multiscale simulation method for self-organization of nanoparticles in dense suspension. J. Comput. Phys. **223**, 108–120 (2007)
Hamaker, H.: The London-van der Waals attraction between spherical particles. Physica **4**, 1058–1072 (1937)
Ho, C.A., Sommerfeld, M.: Modelling of micro-particle agglomeration in turbulent flows. Chem. Eng. Sci. **57**, 3073–3084 (2002)
Israelachvili, J.N.: Intermolecular and Surface Forces. Academic Press Inc., London (1992)
Jain, R., Tschisgale, S., Fröhlich, J.: A collision model for DNS with ellipsoidal particles in viscous fluid. Int. J. Multiph. Flow **120**, 103087 (2019)
Jain, R., Tschisgale, S., Frohlich, J.: A collision model for DNS with ellipsoidal particles in viscous fluid [Corrigendum]. Int. J. Multiph. Flow **150**, 104009 (2022)
Janin, J., Duval, F., Friess, C., Sagaut, P.: A new linear forcing method for isotropic turbulence with controlled integral length scale. Phys. Fluids **33**, 045127 (2021)
Kuerten, J.: Point-particle DNS and LES of particle-laden turbulent flow—a state-of-the-art review. Flow Turbul. Combust. **97**, 689–713 (2016)
Lucci, F., Ferrante, A., Elghobashi, S.: Modulation of isotropic turbulence by particles of Taylor length-scale size. J. Fluid Mech. **650**, 5–55 (2010)
Lundgren, T.S.: Linearly forced isotropic turbulence, pp. 461–473. Stanford University, Centre for Turbulence Research, Annual Research Briefs (2003)
Mallouppas, G., George, W.K., van Wachem, B.G.: New forcing scheme to sustain particle-laden homogeneous and isotropic turbulence. Phys. Fluids **25**, 083304 (2013)
Mandø, M., Yin, C., Sørensen, H., Rosendahl, L.: On the modelling of motion of non-spherical particles in two-phase flow. In: 6th International Conference on Multiphase Flow (2007)
Marchioli, C., Soldati, A., Kuerten, J.G.M., Arcen, B., Taniere, A., Goldensoph, G., Squires, K.D., Cargnelutti, M.F., Portela, L.: Statistics of particle dispersion in direct numerical simulations of wall-bounded turbulence: results of an international collaborative benchmark test. Int. J. Multiph. Flow **34**, 879–893 (2008)
Mark, A., van Wachem, B.G.M.: Derivation and validation of a novel implicit second-order accurate immersed boundary method. J. Comp. Phys. **227**, 6660–6680 (2008)
Mortimer, L.F., Njobuenwu, D.O., Fairweather, M.: Agglomeration dynamics in liquid-solid particle-laden turbulent channel flows using an energy-based deterministic approach. Phys. Fluids **32**, 043301 (2020)
Mortimer, L.F., Fairweather, M.: Assessment of behavioral modification techniques through immersed boundary method simulation of binary particle interactions in isotropic turbulence. Phys. Fluids **33**, 073307 (2021)
Njobuenwu, D.O., Fairweather, M.: Dynamics of single, non-spherical ellipsoidal particles in a turbulent channel flow. Chem. Eng. Sci. **123**, 265–282 (2015)
Peskin, C.: The immersed boundary method. Acta Numer. **11**, 479–517 (2002)
Rosales, C., Meneveau, C.: Linear forcing in numerical simulations of isotropic turbulence: Physical space implementations and convergence properties. Phys. Fluids **17**, 095106 (2005)
Schiller, P., Krüger, S., Wahab, M., Mögel, H.-J.: Interactions between spheroidal colloidal particles. Langmuir **27**, 10429–10437 (2011)
Shardt, O., Derksen, J.J.: Direct simulations of dense suspensions of non-spherical particles. Int. J. Multiph. Flow **47**, 25–36 (2012)

Soldati, A., Marchioli, C.: Physics and modelling of turbulent particle deposition and entrainment: Review of a systematic study. Int. J. Multiph. Flow **35**, 827–839 (2009)
Squires, K., Eaton, J.: Preferential concentration of particles by turbulence. Phys. Fluids **3**, 1169–1178 (1991)
Trojanowicz, M., Kołacinska, K., Grate, J.W.: A review of flow analysis methods for determination of radionuclides in nuclear wastes and nuclear reactor coolants. Talanta **183**, 70–82 (2018)
Uhlmann, M.: An immersed boundary method with direct forcing for the simulation of particulate flows. J. Comput. Phys. **209**, 448–476 (2005)
Verwey, E.J.W., Overbeek, J.T.G.: Theory of the stability of lyophobic colloids. J. Colloid Sci. **10**, 224–225 (1955)
Voth, G., Soldati, A.: Anisotropic particles in turbulence. Ann. Rev. Fluid Mech. **49**, 249–279 (2017)
Wolde, B., Mortimer, L.F., Fairweather, M.: Stokes number effects on deposition in particle-laden turbulent pipe flows. Chem. Eng. Technol. **46**, 1351–1361 (2023)